INTERNATIONAL JOURNAL FOR NUMERICAL METHODS IN FLUIDS, VOL. 14, 1453–1472 (1992)

NUMERICAL SIMULATION OF JET-FORCED FLOW IN A CIRCULAR RESERVOIR USING DISCRETE AND RANDOM VORTEX METHODS

A. G. L. BORTHWICK

Department of Engineering Science, University of Oxford, Oxford OX1 3PJ, U.K.

AND

R. W. BARBER

Department of Civil Engineering, University of Salford, Salford M5 4WT, U.K.

SUMMARY

This paper describes a Biot–Savart discrete vortex model for simulating the flow patterns which occur when a single high-velocity inflow jet is used to stir the fluid within a circular container. The first stage of the model consists of conformally mapping the circular perimeter of the container onto a rectangle by means of a Schwarz–Christoffel transformation. A potential flow solution is then obtained for the flow inside the rectangle and this is transformed to give the potential flow inside the circle. In the second stage of the simulation, discrete vortices are added at the inlet of the physical system in order to model the inflow shear layers. Velocity components resulting from the discrete vortices and their images in the walls of the cylinder are superimposed on the uniform potential flow solution. The positions of the vortices are updated using a Lagrangian tracking procedure. Viscous effects are incorporated through the use of random walks. From the results it is shown that the discrete vortex method does predict qualitatively the important features of jet-forced reservoir flow.

KEY WORDS Discrete vortices Random walks Conformal mapping Reservoir flow

INTRODUCTION

Discrete vortex models offer a powerful computational technique for the simulation of two-dimensional viscous flows, particularly in cases where separation or vortex roll-up occurs. Helmholtz[1] laid the foundation for such models by showing that in 'an inviscid fluid a vortex tube moves with the fluid and its strength remains constant'. Using a small number of discrete vortices, Rosenhead[2] demonstrated the feasibility of the method for the case of contraflowing streams. However, it was only when computers became available that the number of elemental vortices could be increased sufficiently to allow adequate simulation of the complex shear layers in wakes and jets. Even so, instabilities which arise from the discretization of vorticity tend to disrupt vortex motions after some time; consequently, many smoothing techniques are to be found in the literature, not all of them leading to desirable results. It is the intention of this introduction to summarize briefly the developments that have been made since Rosenhead's pioneering work. For detailed expositions of the discrete vortex method the reader is referred to comprehensive review articles by Clements and Maull[3] and Sarpkaya.[4]

0271–2091/92/121453–20$10.00

Received February 1991
Revised November 1991

Research into the application of discrete vortices began with Rosenhead,[2] who studied the surface instability between two streams travelling in opposite directions. He replaced the continuous sheet of vorticity between the two layers by 12 elemental vortices per wavelength and then used a time-stepping finite difference procedure to calculate the deformation of the vortex sheet due to the mutually induced velocities at each vortex position. Although the simulation was only continued for four time steps (since the calculation was performed by hand), the results clearly showed the vortex sheet rolling up into clusters of vortices. Later, Birkhoff and Fisher[5] increased the number of vortices per wavelength to 22 and repeated Rosenhead's study, but with smaller time increments. They found that chaotic motions eventually occurred, caused by the singular nature of the self-induced velocity field due to the positions of the vortices; in other words, the closer the discrete vortices came together, the greater their propensity to shoot off or orbit about each other.

Early applications of the discrete vortex method to aerodynamics consisted of modelling wing tip vortices. For example, Westwater[6] used discrete vortex calculations to show that roll-up of the trailing vortex sheet began at the wing tips. Takami[7] and Moore[8] repeated Westwater's calculations and found that chaotic motions could also occur in this case. Since then, a variety of attempts have been made to overcome the instabilities which arise when discrete vortices come too close to each other. Kuwahara and Takami[9] controlled the irregular roll-up by using Rankine-type vortices with expanding cores. Clements and Maull[10] calmed vortex motions by amalgamating vortices on the basis of their velocities. Moore[11] introduced a single tip vortex to represent the rolled-up inner region.

Abernathy and Kronauer[12] modelled the interaction of two free shear layers with discrete vortices and simulated the development of a typical von Kármán vortex street; this was the precursor to the use of the technique for simulating two-dimensional flows past obstacles. Several authors, including Gerrard,[13] Sarpkaya,[14] Laird,[15] Chaplin,[16] Stansby[17] and Sarpkaya and Schoaff,[18] modelled the flow past a circular cylinder using discrete vortices superimposed on the potential flow solution. Varying degrees of complexity for introducing the nascent vortices were devised, ranging from a fixed point of introduction (e.g. References 13, 15 and 16) to a variable separation point (e.g. References 14, 17 and 18). Flows past square-ended bluff bodies were considered by Clements[19] and Clements and Maull,[3] who utilized fixed nascent vortex positions since separation would always occur at the sharp corners of the obstacle. Clements[19] mapped the flow region surrounding the square-ended bluff body onto an upper half-plane stretching to infinity. He achieved this by use of a conformal Schwartz–Christoffel transformation and then corrected the vortex velocities according to Routh's rule.

All the early discrete vortex simulations employed pure Lagrangian numerical schemes to advect vorticity. Individual velocities of the discrete vortices were determined by summing the velocity contributions from all the vortices in the field and superimposing the resultant on the potential flow solution. For this reason the technique is often described as the 'direct summation method'. The methodology may also be referred to as a Biot–Savart approach on account of the similarity between the magnetic field intensity caused by an electric current and the velocity induced by a vortex element.

The advantage of the Biot–Savart technique is that it is entirely independent of grid-based numerical methods, thereby eliminating artificial diffusion usually associated with Eulerian finite difference schemes. There are, however, two main difficulties with the method. First, the elemental vortices have singularities at their centres of rotation which produce extremely large velocities in the immediate vicinity of each vortex. This can cause instabilities in the simulation of the roll-up of a vortex sheet. As the vortices in the centre of a cluster move closer to each other, there is a tendency for them to orbit around themselves in a chaotic manner rather than to roll-up into the

expected spiral. In order to overcome this particular difficulty, various 'cut-off' schemes have been devised to desingularize the velocity field at the centres of the vortices; examples include Chorin and Bernard's[20] vortex 'blob' and Chaplin's[16] use of Rankine vortices. The second disadvantage with the Biot–Savart approach is that the number of arithmetic operations required to update the vortex positions by one time step is approximately proportional to N^2, where N is the number of vortices. Thus the computational time required per time step increases dramatically as further vortices are added. One method which partially overcomes this difficulty is to use a computer algorithm to amalgamate vortices if they are closer than a certain distance apart. Not only does this help to alleviate the computational costs but it can also remove the propensity of vortices to orbit one another.

The dependence of the Biot–Savart approach upon a work load proportional to N^2 implies that the technique is unable to cope with large numbers of vortices. Consequently, from the late 1970s a 'hybrid' Lagrangian–Eulerian discrete vortex method has been increasingly used instead of the direct summation approach (e.g. References 21–23). The technique is referred to as the vortex-in-cell (VIC) method and employs a Lagrangian method to track the vortex positions and an Eulerian grid-based finite difference scheme to solve the elliptic streamfunction equation defining the velocity field. Undoubtedly, the main advantage with the vortex-in-cell approach is that the cost of the computational technique is linear in N. This allows the method to use a larger number of vortices. Furthermore, the bilinear interpolation technique (which is utilized during the apportionment of vorticity to the nodes of the computational mesh) effectively removes the singularity in the velocity field without having to resort to vortex 'blobs' or Rankine vortices. However, the drawback with the VIC technique is that the grid independence of the original Biot–Savart approach has been abandoned. Furthermore, savings from the removal of the N^2 cost constraint may be completely destroyed if a very fine grid is employed, owing to the computationally expensive Poisson solver. As pointed out by Sarpkaya,[4] 'classical' Biot–Savart techniques therefore still have an important role to play in discrete vortex modelling.

This paper implements a Biot–Savart discrete vortex model for calculating two-dimensional jet-forced flow within a flat-bottomed circular reservoir and follows the methodology adopted by Borthwick *et al.*[24] Figure 1 illustrates the problem formulation and shows a typical asymmetrical circular reservoir with a single inlet and a single outlet. The radial inflow jet produces separation at the sharp inlet corner points, and the shear layers which are formed cause two recirculating

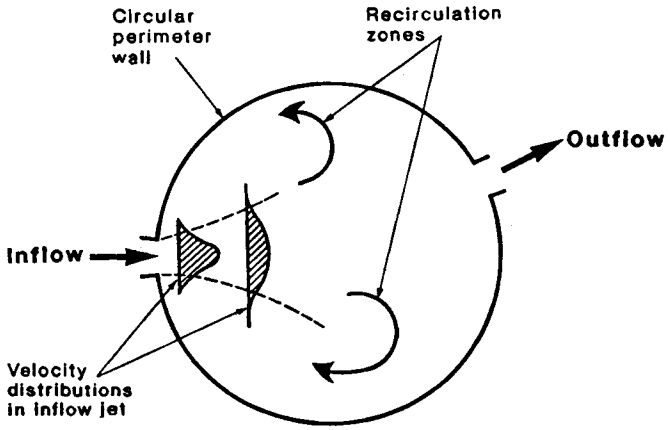

Figure 1. Problem formulation

eddies (of opposite senses of rotation) to develop either side of the main throughflow. The flow pattern is of interest in that it is representative of conditions encountered in a water supply service reservoir. Usually the flow passes directly from inlet to outlet with very little mixing in the recirculating zones and consequently there is a tendency for those areas with low velocities to stagnate and become ridden with algae.

Most numerical investigations of radial jet-forced flow within circular tanks and reservoirs have been undertaken using finite difference discretizations of either the streamfunction/vorticity transport equations or the depth-averaged Reynolds equations (e.g. References 25–29). The computational method presented in this paper provides an alternative solution procedure which is theoretically free from grid-induced numerical diffusive effects.

NUMERICAL SCHEME

Irrotational flow solution

A two-stage conformal mapping is used to transform the circular flow domain onto a rectangle. This allows the potential flow to be determined analytically. Figure 2 shows the physical domain R located at the origin of the complex z-plane, $z=x+\mathrm{i}y$, where $\mathrm{i}=\sqrt{(-1)}$. The flow problem is non-dimensionalized and therefore the reservoir is represented by a unit circle. Points a, b, c and d on the perimeter of the cylinder define the inlet and outlet corners.

During the first stage of the mapping procedure (illustrated in Figure 2) the circular reservoir is transformed onto the upper half of the s-plane ($s=p+\mathrm{i}q$) using the function

$$s=-\mathrm{i}\left(\frac{z-\mathrm{i}}{z+\mathrm{i}}\right), \tag{1}$$

which may be rewritten in terms of the co-ordinates x and y as

$$s=-\mathrm{i}\left(\frac{x^2+y^2-1-2\mathrm{i}x}{x^2+y^2+2y+1}\right). \tag{2}$$

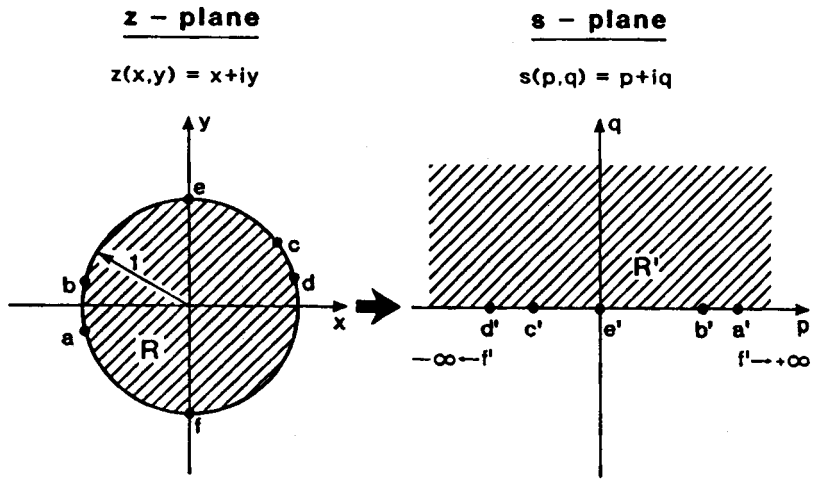

Figure 2. Conformal mapping, step 1: z-plane to s-plane

On the perimeter of the circle $x^2+y^2=1$ and therefore

$$s=p+\mathrm{i}q=-\mathrm{i}\left(\frac{-2\mathrm{i}x}{2+2y}\right). \tag{3}$$

Thus on the circumference of the reservoir

$$p=-\frac{x}{1+y} \quad \text{and} \quad q=0, \tag{4}$$

and consequently the perimeter wall is mapped onto the $q=0$ axis. The points a', b', c' and d' in Figure 2 represent the images of the corner locations after the transformation.

The second stage of the conformal mapping employs a Schwarz–Christoffel transformation to convert the upper half of the s-plane into a rectangular region in the ζ-co-ordinate frame ($\zeta=\eta+\mathrm{i}\xi$). Figure 3 illustrates the mapping and shows the inlet and outlet openings $a''b''$ and $c''d''$ forming opposite sides of the rectangular region R''. The Schwarz–Christoffel transformation is defined by

$$\frac{\mathrm{d}\zeta}{\mathrm{d}s}=A(s-p_1)^{\alpha_1/\pi-1}(s-p_2)^{\alpha_2/\pi-1}\cdots(s-p_n)^{\alpha_n/\pi-1}, \tag{5}$$

where A is an arbitrary constant, $\alpha_1, \alpha_2, \ldots, \alpha_n$ are the interior angles of the region in the ζ-plane, $p_1, p_2, \ldots, p_n$ are the p-values of the corner nodes and n is the total number of vertices. In this particular case $n=4$ and $\alpha_1=\alpha_2=\alpha_3=\alpha_4=\pi/2$. Assuming A to be unity allows the transformation to be simplified to

$$\frac{\mathrm{d}\zeta}{\mathrm{d}s}=\frac{1}{\sqrt{[(s-a')(s-b')(s-c')(s-d')]}}. \tag{6}$$

The next stage of the numerical scheme involves generating a uniform potential flow within the rectangular region R''. This is achieved by equating the η- and ξ-co-ordinates to the velocity

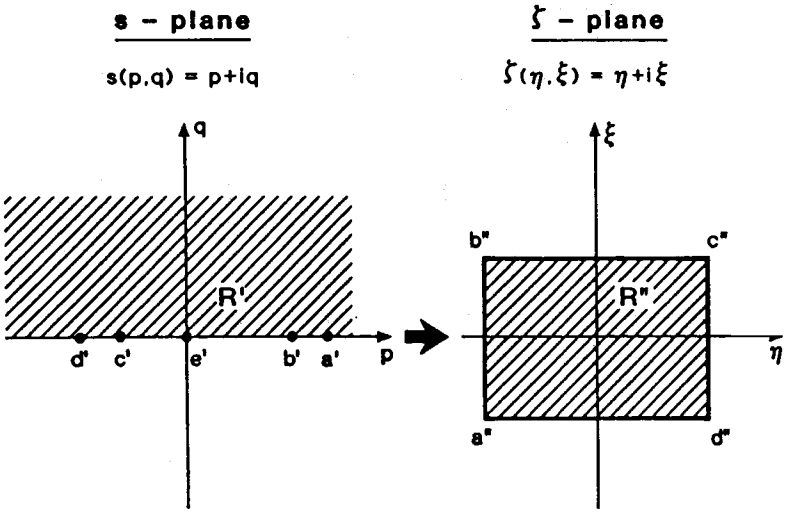

Figure 3. Conformal mapping, step 2: s-plane to ζ-plane

potential Φ and the streamfunction ψ respectively. Thus the complex potential $\omega = \Phi + i\psi$ is equal to ζ.

The complex velocity v is defined as

$$v = \frac{\partial \omega}{\partial x} = \frac{\partial \Phi}{\partial x} + i\frac{\partial \psi}{\partial x} = u - iv, \tag{7}$$

where u and v are the velocity components in the x- and y-directions respectively. Using the chain rule, the complex velocity may be expressed as

$$v = \frac{\partial \omega}{\partial x} = \frac{d\omega}{dz}\frac{\partial z}{\partial x}. \tag{8}$$

However, $\partial z/\partial x = 1$ and, since the complex potential is equal to ζ,

$$v = \frac{d\omega}{dz} = \frac{d\zeta}{dz}. \tag{9}$$

The potential flow solution in the physical z-plane can therefore be determined by using the chain rule to expand $d\zeta/dz$, i.e.

$$v = \frac{d\zeta}{dz} = \frac{d\zeta}{ds}\frac{ds}{dz}. \tag{10}$$

Differentiating equation (1) with respect to z yields

$$\frac{ds}{dz} = \frac{2}{(z+i)^2}. \tag{11}$$

Hence the complex velocity at any point in the circular reservoir may be found by substituting equations (11) and (6) into (10) to give

$$v = u - iv = \frac{1}{\sqrt{[(s-a')(s-b')(s-c')(s-d')]}}\frac{2}{(z+i)^2}. \tag{12}$$

The complex velocity presented in the above expression must be scaled so that the average velocity across the inlet of the physical domain is unity. This is achieved by dividing equation (12) by the unscaled discharge Q and multiplying by the inlet width L. The unscaled discharge through the reservoir is given by the difference in streamfunction values between the two inlet corner points at a'' and b''. Since a'' and b'' lie on the same equipotential line,

$$Q = \psi_{b''} - \psi_{a''} = \frac{1}{i}(\zeta_{b''} - \zeta_{a''}) = \frac{1}{i}\int_{a'}^{b'}\frac{d\zeta}{ds}\,ds. \tag{13}$$

The limits of this integral lie on the real axis of the s-plane and so the integrand can be expressed entirely in terms of p. After rearrangement the unscaled discharge becomes

$$Q = \int_{b'}^{a'}\frac{dp}{\sqrt{[(a'-p)(p-b')(p-c')\ (p-d')]}}. \tag{14}$$

The above equation is an incomplete elliptic integral of the first kind and may be rewritten according to Byrd and Friedman[30] as

$$Q = tF(\lambda, r), \tag{15}$$

where

$$t=\frac{2}{\sqrt{[(a'-c')(b'-d')]}},$$

$$\lambda=\sin^{-1}\left[\sqrt{\left(\frac{(a'-c')(p-b')}{(a'-b')(p-c')}\right)}\right]=\frac{\pi}{2} \quad \text{for } p=a',$$

$$r=\sqrt{\left(\frac{(a'-b')(c'-d')}{(a'-c')(b'-d')}\right)}.$$

F is a complete elliptic integral of the first kind and may be evaluated as a series approximation:

$$Q=tF(\pi/2, r)=t\frac{\pi}{2}\left[1+\left(\frac{1}{2}\right)^2 r^2+\left(\frac{1\cdot3}{2\cdot4}\right)^2 r^4+\left(\frac{1\cdot3\cdot5}{2\cdot4\cdot6}\right)^2 r^6+\ldots\right]. \tag{16}$$

Thus the scaled uniform complex velocity v_s for the irrotational flow solution is given by

$$v_s=u_s-\mathrm{i}v_s=\frac{L}{Q}\frac{1}{\sqrt{[(s-a')(s-b')(s-c')(s-d')]}}\frac{2}{(z+\mathrm{i})^2}, \tag{17}$$

where u_s and v_s are the scaled velocity components in the x- and y-directions respectively.

Discrete vortex simulation

The shear layers formed between the inflow jet and the inlet boundary are modelled by adding discrete vortices to the irrotational flow solution of equation (17). If the simulation employs potential vortices, the complex velocity due to the superposition of the scaled uniform irrotational flow and the vortices is given by

$$u-\mathrm{i}v=v_s-\frac{\mathrm{i}}{2\pi}\sum_{j=1}^{N}\frac{\Gamma_j}{z-z_j}+\frac{\mathrm{i}}{2\pi}\sum_{j=1}^{N}\frac{\Gamma_j}{z-1/\bar{z}_j}, \tag{18}$$

where Γ_j is the circulation of the jth vortex (positive for anticlockwise rotation), z_j is the position of the jth vortex, N is the total number of vortices in the flow field and the overbar denotes a complex conjugate. The velocity field due to the vortices is calculated as two separate summations: the first is the velocity contribution from the actual vortices, whilst the second arises from the fact that each vortex must have an image of opposite circulation at the 'inverse' position *outside* the reservoir. These vortex images ensure that the cylinder surface remains a streamline.[31]

The singularity at the centre of a potential vortex may induce excessive velocities when two vortices approach each other; following Chaplin,[16] this difficulty is overcome through the use of Rankine vortices. Thus the complex velocity at the point $z=x+\mathrm{i}y$ becomes

$$u-\mathrm{i}v=v_s-\frac{\mathrm{i}}{2\pi}\sum\frac{\Gamma_j}{z-z_j}+\frac{\mathrm{i}}{2\pi}\sum\frac{\Gamma_j}{z-1/\bar{z}_j}-\frac{\mathrm{i}}{2\pi r_0^2}\sum\Gamma_j\overline{(z-z_j)}+\frac{\mathrm{i}}{2\pi r_0^2}\sum\Gamma_j\overline{(z-1/\bar{z}_j)}, \tag{19}$$

where r_0 is the radius of the vortex core. The first summation is utilized for vortices whose cores do not cover the point z, whilst the third summation is taken over the remaining vortices. Rankine velocity profiles are also used for the vortex images. Therefore the second summation is employed whenever the core of an image vortex does not enclose the point z, whereas the fourth summation is used if z lies within the image core.

Introduction of nascent vortices

The strengths of the vortices used to simulate the shear layers of the inflow jet are found from a consideration of the vorticity flux across the inlet boundary layers. Figure 4 illustrates the assumed velocity profile across the inflow and defines a co-ordinate system with x' and y' measured parallel and perpendicular to the lower inlet wall. The vorticity flux across the boundary layer is given approximately by Raudkivi and Callander[32] as

$$\frac{d\Gamma}{dt}=\int_0^{\delta} u'\omega\, dy' = -\tfrac{1}{2}U^2, \tag{20}$$

where u' is the velocity component in the x'-direction, ω is the vorticity, δ is the nominal thickness of the boundary layer and U is the free stream velocity. In the discrete vortex model the vorticity flux across the boundary layer is equivalent to the circulation of an individual discrete vortex, Γ_j, divided by the time increment Δt_v between the introduction of nascent vortices. Since the inflow velocity has been non-dimensionalised ($U=1$), the strength of vortices originating from the lower boundary layer can thus be expressed as

$$\Gamma_j = -\frac{\Delta t_v}{2}, \tag{21}$$

where the circulation Γ_j is positive for anticlockwise rotation. The vortices introduced at the upper boundary separation point are calculated in a similar manner:

$$\Gamma_j = \frac{\Delta t_v}{2}, \tag{22}$$

Vortex tracking

As explained in the Introduction, the computer time necessary to update the vortex positions in a Biot–Savart approach is approximately proportional to N^2, where N is the number of vortices. This is because the velocity of an individual vortex is found by summing the velocity contributions from each of the remaining $N-1$ vortices. In order to avoid using excessive computer

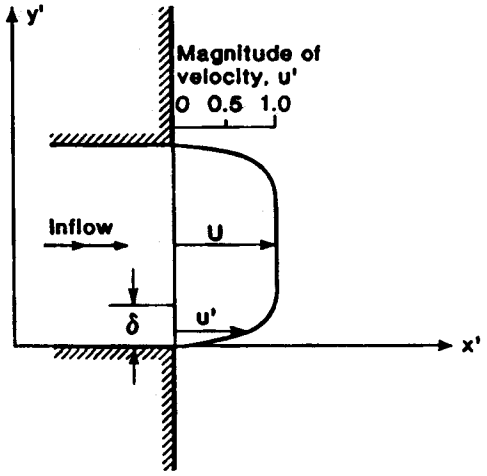

Figure 4. Assumed two-dimensional velocity profile at inlet (after Borthwick *et al.*[24])

resources, the time increment Δt_v between the addition of nascent vortices must be carefully chosen. Numerical experimentation has revealed that a suitable value of Δt_v from the viewpoint of computer CPU time is generally too large for the finite difference vortex-tracking discretization; vortices near the circular perimeter of the reservoir are frequently transported across the boundary wall. Consequently, a smaller time step Δt_m is employed to update the vorticity field. For convenience, Δt_v is chosen to be a multiple of Δt_m so that the addition of new vortices at the inlet will coincide with time increments employed in the Lagrangian tracking procedure.

The vortex positions are advanced over the 'vortex movement' time step Δt_m using a first-order-accurate finite difference scheme:

$$x_j(t+\Delta t_m)=x_j(t)+u_j(t)\,\Delta t_m, \qquad y_j(t+\Delta t_m)=y_j(t)+v_j(t)\,\Delta t_m, \tag{23}$$

where u_j and v_j are the velocity components of the jth vortex (determined from either equation (18) or (19)). In the event of a vortex being advected across a solid perimeter wall, it is 'reflected' back into the flow domain. Vortices which leave through the outlet of the reservoir are removed from subsequent flow calculations.

Random walk

The vortex-tracking scheme presented above models only the advective processes of the discretized vorticity field. Chorin[33] proposed that the viscous effects could be simulated by treating the diffusive and advective phenomena in separate numerical procedures. This is equivalent to replacing the exact vorticity transport equation (simultaneous advection and diffusion of vorticity)

$$\frac{D\omega}{Dt}=\frac{\partial\omega}{\partial t}+\mathbf{u}\cdot\nabla\omega=\nu\nabla^2\omega \tag{24}$$

by two *sequential* equations,

$$\frac{\partial\omega}{\partial t}+\mathbf{u}\cdot\nabla\omega=0 \tag{25a}$$

and

$$\frac{\partial\omega}{\partial t}=\nu\nabla^2\omega, \tag{25b}$$

where $\mathbf{u}$ represents the velocity *vector*.

A stochastic technique is used to model the pure diffusion of equation (25b); at the end of the advective tracking stage, each vortex undergoes a random walk in two orthogonal directions. The standard deviation of these random walks must be compatible with the analytical solution of the diffusion equation and therefore the fluctuating random velocity components of a vortex are generated as[33]

$$u_r=r_1\left(\frac{2\nu}{\Delta t_m}\right)^{1/2}, \qquad v_r=r_2\left(\frac{2\nu}{\Delta t_m}\right)^{1/2}, \tag{26}$$

where ν is the eddy viscosity and r_1 and r_2 are *independent* normally distributed random numbers each with zero mean and standard deviation of unity. For convenience the computer model is based upon the length of the random walks. Hence equations (26) are recast as

$$\Delta x_r=u_r\Delta t_m=r_1(2\nu\Delta t_m)^{1/2}, \qquad \Delta y_r=v_r\Delta t_m=r_2(2\nu\Delta t_m)^{1/2}, \tag{27}$$

where Δx_r and Δy_r are the random walk *distances* in the x- and y-directions respectively. Once the vortices have been advanced by random walks, the boundary of the reservoir is preserved as a circle by implicit repositioning of the image vortices according to the Milne-Thomson theorem.[31] Any tendency for vortices to cross the boundary because of a high value of mutually induced velocity from a nearby vortex was minimized by appropriate reduction in the time step Δt_m. As mentioned previously, any vortex which did cross the boundary was given an additional compensatory radial displacement to reflect it back into the reservoir.

OPTIMIZATION OF EMPIRICAL FLOW PARAMETERS

The previous section has described a Biot–Savart discrete vortex model for simulating two-dimensional jet-forced flows in flat-bottomed circular reservoirs. Although the governing equations originate from well-defined physical principles, the computer model requires the user to select appropriate values for a number of important parameters. The success of the simulation depends crucially upon three variables: the exact position of introduction of the nascent vortices, the time increment Δt_v between successive additions of new vortices and the time step Δt_m used in the Lagrangian tracking procedure. Furthermore, the 'smoothness' of the velocity vector diagrams depicting the reservoir flow is influenced by the use of either Rankine or potential vortices. Selection of the various empirical parameters is accomplished by conducting extensive numerical trials.

Borthwick *et al.*[24] have previously outlined the method employed to select the positions of vortex introduction. Figure 5 depicts the velocity profile across the inlet of the reservoir as determined by the numerical model and shows that the most obvious defect in the potential flow solution is the complete absence of a boundary layer. Instead, potential flow theory predicts a velocity profile which tends asymptotically to infinity either side of the inlet. Consequently, the transport of nascent vortices into the interior of the cylinder is dominated by the high velocities at the edges of the jet. The closer new vortices are introduced to the inlet corners, the more rapidly they enter the reservoir. This forces the numerical scheme to adopt a smaller time step in the Lagrangian tracking procedure and so increases the computational costs of the simulation. In the present study the vortex introduction positions are located one-hundredth of the distance across the inlet.

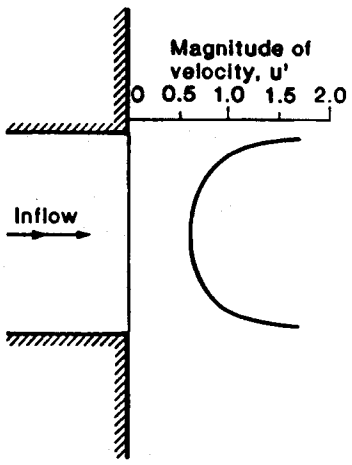

Figure 5. Computed velocity profile at inlet

The time interval Δt_v between successive additions of new vortices at the inlet separation points is the primary factor which governs the overall run time of the model. In order that the simulation can employ a large number of vortices, Δt_v is chosen to be as *small* as possible whilst maintaining a sensible overall run time. The numerical experiments to discover the optimum value for Δt_v were coupled with those used to find a suitable 'vortex movement' time increment Δt_m. If large values of Δt_m are employed, vortices approaching the outlet often attempt to cross the solid perimeter wall; this demonstrates that vortices are not being tracked along the correct streamlines and indicates that a reduction in Δt_m is necessary. After many trial runs the non-dimensional time increments Δt_v and Δt_m were chosen to be 0·1 and 0·002 respectively. These values produced acceptable flow simulations and allowed the computer model to be advanced to the non-dimensional time level of $t = 10{\cdot}0$ in approximately 240 min of CPU time on a PR1ME 9955 computer.

The selection of the size of core for the Rankine vortices is a more arbitrary decision. Chaplin[16] studied the flow past a circular cylinder of unit diameter and chose to use Rankine vortices having a core radius r_0 equal to 0·1. In the present numerical study the discrete vortex method is applied to the confined flow *within* a circular cylinder. Since the inlet width of the reservoir in the Results section is equal to $\pi/16 (= 0{\cdot}196)$, it was judged that the core radius should be smaller than that employed by Chaplin. Trial and error eventually led to the adoption of a core radius r_0 equal to 0·05. This proved large enough to remove the excessive velocities close to the vortex centres whilst enabling the vortex positions at the early time stages of the calculation to resemble a potential vortex simulation.

RESULTS

Borthwick *et al.*[24] have already presented results from a Biot–Savart discrete vortex model for simulating flows in circular tanks and reservoirs. They considered two separate geometries: the first case consisted of an inlet $\pi/2$ radians anticlockwise from the outlet, whereas the second geometry represented a reservoir having an inlet diametrically opposite the outflow opening. The computer model described herein extends Borthwick *et al.*'s investigation to include Rankine vortices and a random walk mechanism (to simulate diffusive processes). Test cases corresponding to the geometries studied by Borthwick *et al.* were considered initially in order to validate the numerical algorithms used in the computer code. However, for presentational purposes the results utilize the asymmetrical circular reservoir geometry investigated by Mills[26] and Borthwick and Barber.[29] The inlet and outlet openings subtend an angle of $\pi/16$ radians and their centrelines are separated by $7\pi/8$. Details of the reservoir geometry are given in Table I together with a summary of the values of the semi-empirical flow parameters discussed earlier.

Table I. Reservoir geometry and empirical flow parameters

Inlet co-ordinates	(−0·9952, −0·0980) and (−0·9952, 0·0980)
Outlet co-ordinates	(0·8819, 0·4714) and (0·9569, 0·2903)
Position of vortex introduction	(−0·9952, −0·0961) and (−0·9952, 0·0961)
Strength of vortices	±0·05
Time increment between vortex movement, Δt_m	0·002
Time increment between addition of nascent vortices, Δt_v	0·10
Rankine vortex core size, r_0	0·05

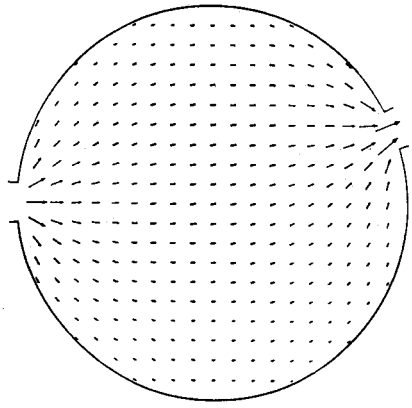

Figure 6. Velocity distribution for irrotational flow

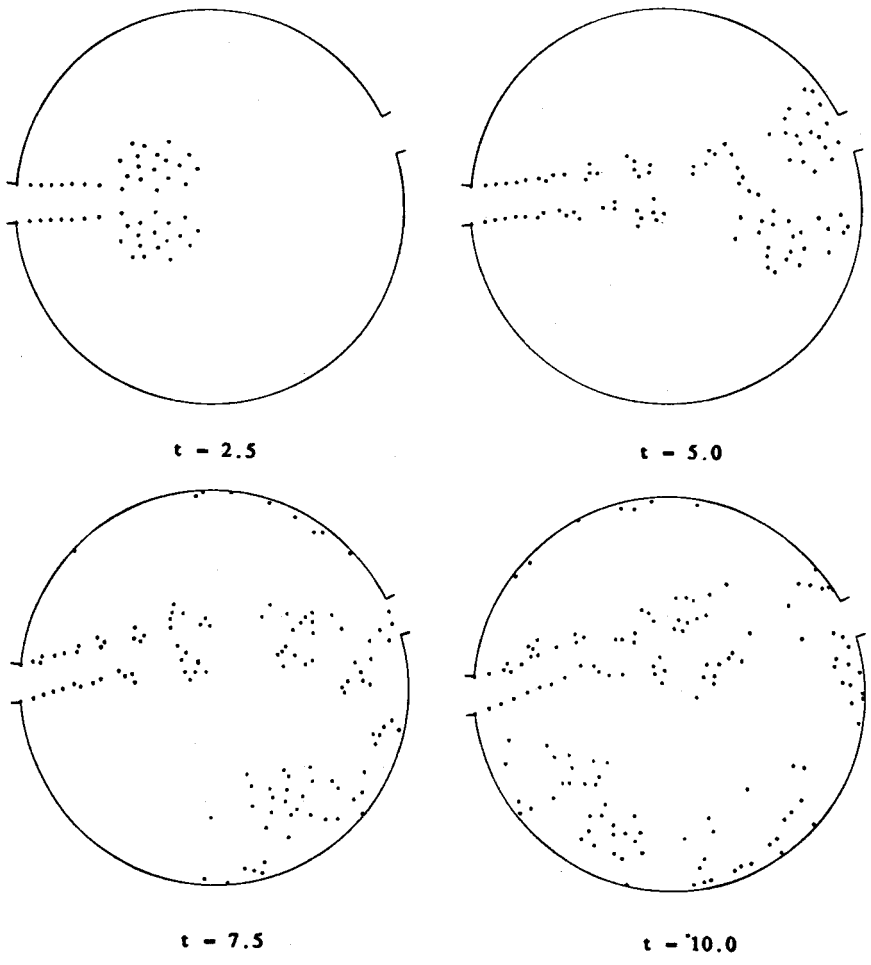

Figure 7. Vortex positions: potential vortex simulation

Figure 6 illustrates the irrotational flow solution determined from the analytical expression given in equation (17); the velocity vectors are scaled so that a length equal to the radius of the cylinder corresponds to a magnitude of 5·0. As a check the irrotational flow solution was also determined numerically from a finite difference discretization of Laplace's equation. The analytical and numerical solutions were identical, confirming the validity of the two-stage conformal mapping procedure.

Figures 7 and 8 depict the sequence of vortex positions and velocity distributions obtained from a 'pure advection' potential vortex simulation, i.e. without the random walk mechanism. (It should be noted that the velocity vectors in Figures 8, 10 and 12 are scaled so that an arrow length equal to the radius of the reservoir corresponds to a magnitude of 10·0.) During the early stages of the calculation vortices enter the reservoir in a symmetrical manner and roll up into two distinct eddies of opposite senses of rotation. By $t = 5{\cdot}0$ part of the eddy formed by the upper shear layer begins to exit the reservoir. The removal of vortices with positive circulation causes the net

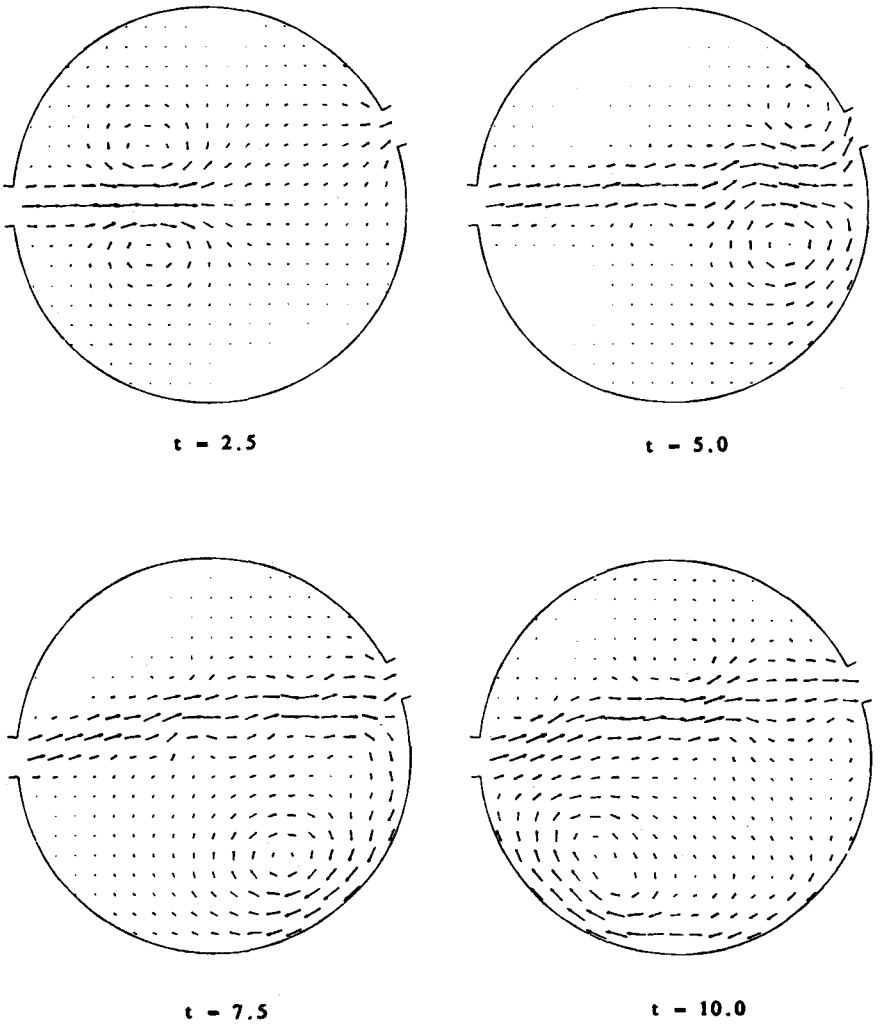

Figure 8. Velocity distributions: potential vortex simulation

vorticity in the reservoir to become negative and accounts for the dominance of the clockwise-rotating lower gyre structure (Figure 8). Between $t = 5{\cdot}0$ and $10{\cdot}0$ the inflow jet realigns itself so that most of the throughflow passes directly between inlet and outlet. In the later stages of the simulation the jet begins to waver as the discrete vortices modelling the shear layers either side of the throughflow assemble into distinct clusters. The strength of the lower eddy increases throughout the calculation as vortices of clockwise rotation are recirculated in the lower gyre. By $t = 10{\cdot}0$ the main region of recirculation has moved back towards the inlet and starts to affect the direction of the inflow jet. Continuation of the simulation beyond $t = 10{\cdot}0$ results in chaotic unrealistic motions which overwhelm the numerical scheme; velocities in the lower eddy increase to unrealistically high values, whilst the upper eddy practically disappears.

Figures 9 and 10 illustrate the results from a simulation employing Rankine vortices with a core radius r_0 equal to 0·05. As for the previous case the computer model tracks the vortices using

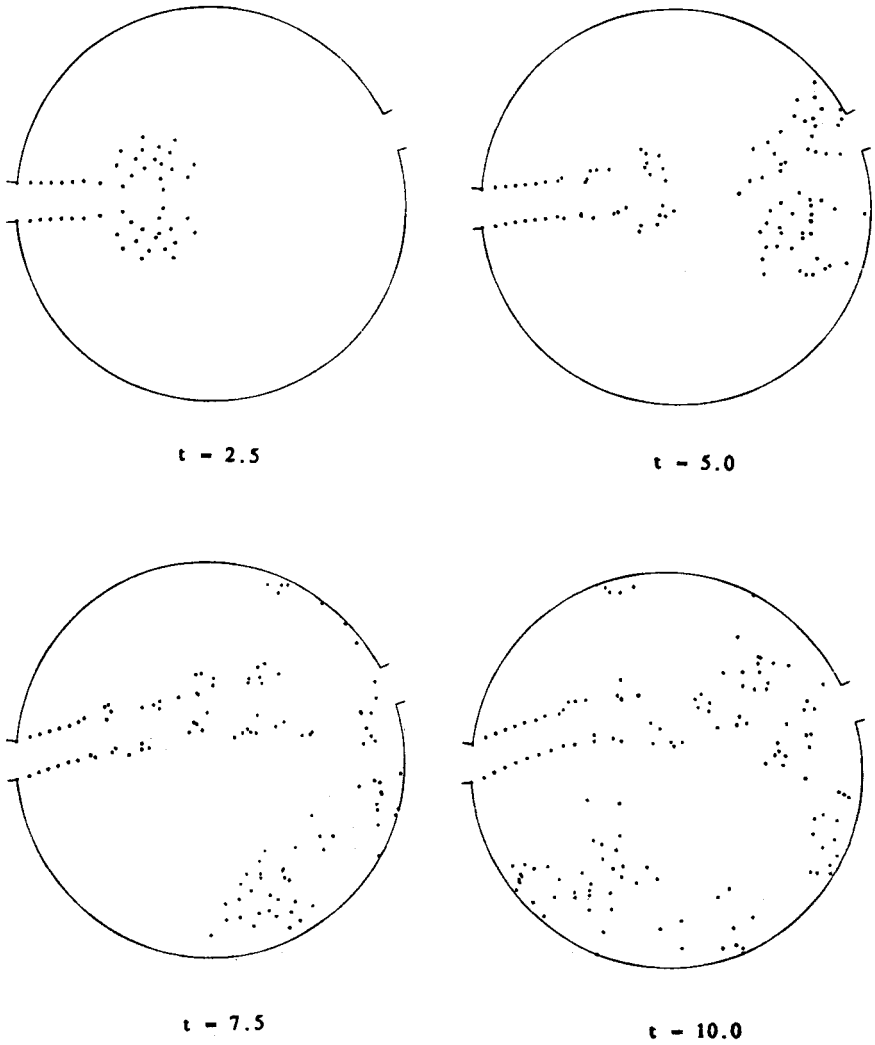

Figure 9. Vortex positions: Rankine vortex simulation ($r_0 = 0{\cdot}05$)

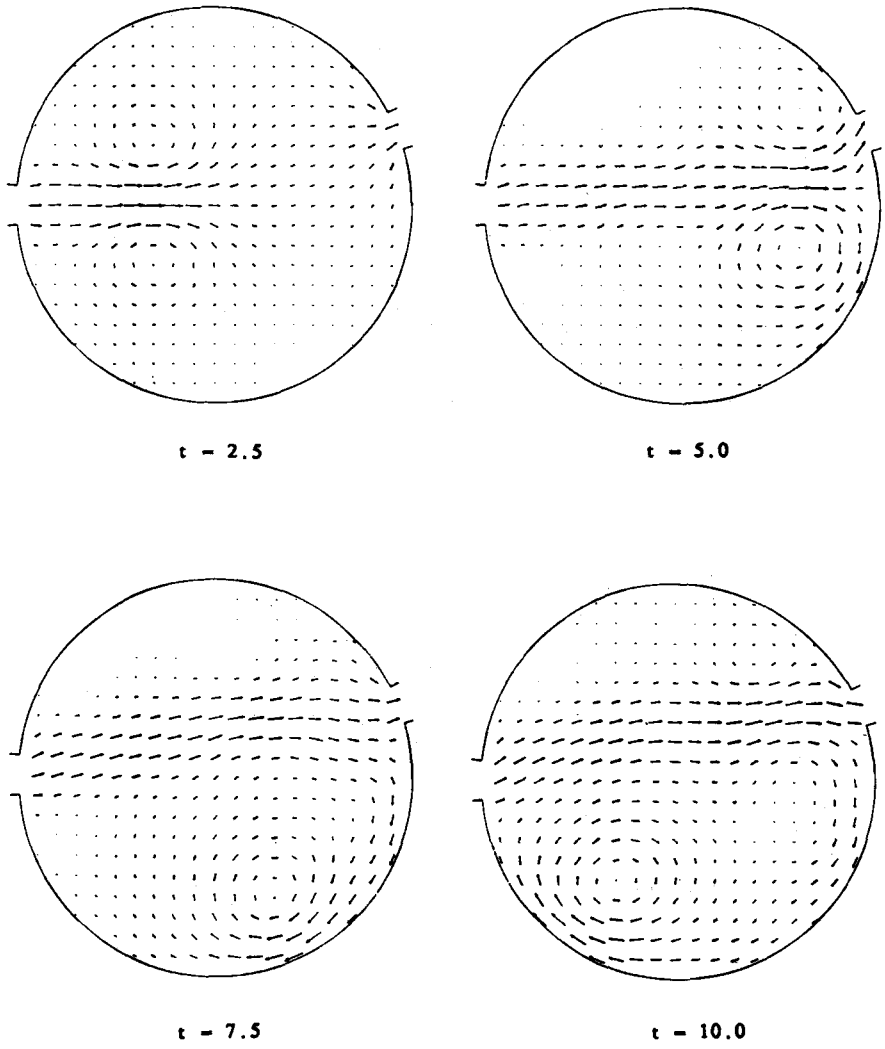

Figure 10. Velocity distributions: Rankine vortex simulation ($r_0 = 0{\cdot}05$)

a pure advective Lagrangian scheme. It can be seen that the vortex positions during the early stages of the flow are almost identical to the potential vortex positions shown in Figure 7. This indicates that the Rankine velocity profiles do not radically alter the discretization of the vorticity field. Figure 10 illustrates the smoothing effect of the Rankine cores by demonstrating that the velocity vectors depicting the flow are much less susceptible to 'distortion' in the vicinity of the vortex centres. Moreover, the use of Rankine velocity profiles reduces the tendency for vortices to be advected across the solid perimeter walls of the flow domain. This can be attributed to the elimination of the large mutually induced velocities which are created when two potential vortices move close to each other. The Rankine vortex model predicts a slightly weaker recirculation zone in the lower portion of the reservoir. However, considering the large core size in relation to the dimensions of the reservoir, the potential and Rankine vortex simulations depicted in Figures 7–10 are remarkably consistent.

The final set of results utilizes Rankine vortices ($r_0 = 0{\cdot}05$) in conjunction with the random walk technique. Figures 11 and 12 show the development of recirculation for an inlet Reynolds number (based upon the horizontal eddy viscosity coefficient) of 100. The inlet Reynolds number is defined in an identical manner to that of Mills,[26] i.e.

$$Re_1 = \frac{U_1 \varepsilon R_0}{\nu}, \tag{28}$$

where U_1 is the mean inlet velocity, ε is half the angle subtended by the inlet, R_0 is the radius of the reservoir and ν is the horizontal eddy viscosity coefficient.

Figure 11 illustrates that the random walk algorithm has a dramatic effect on vortex positions; the symmetrical entry of vortices into the reservoir is completely destroyed and the characteristic roll-up of vortices into two distinct eddies is less well defined. Diffusion of the shear layer manifests itself as a transverse spreading of the vortex positions. Although the individual vortices

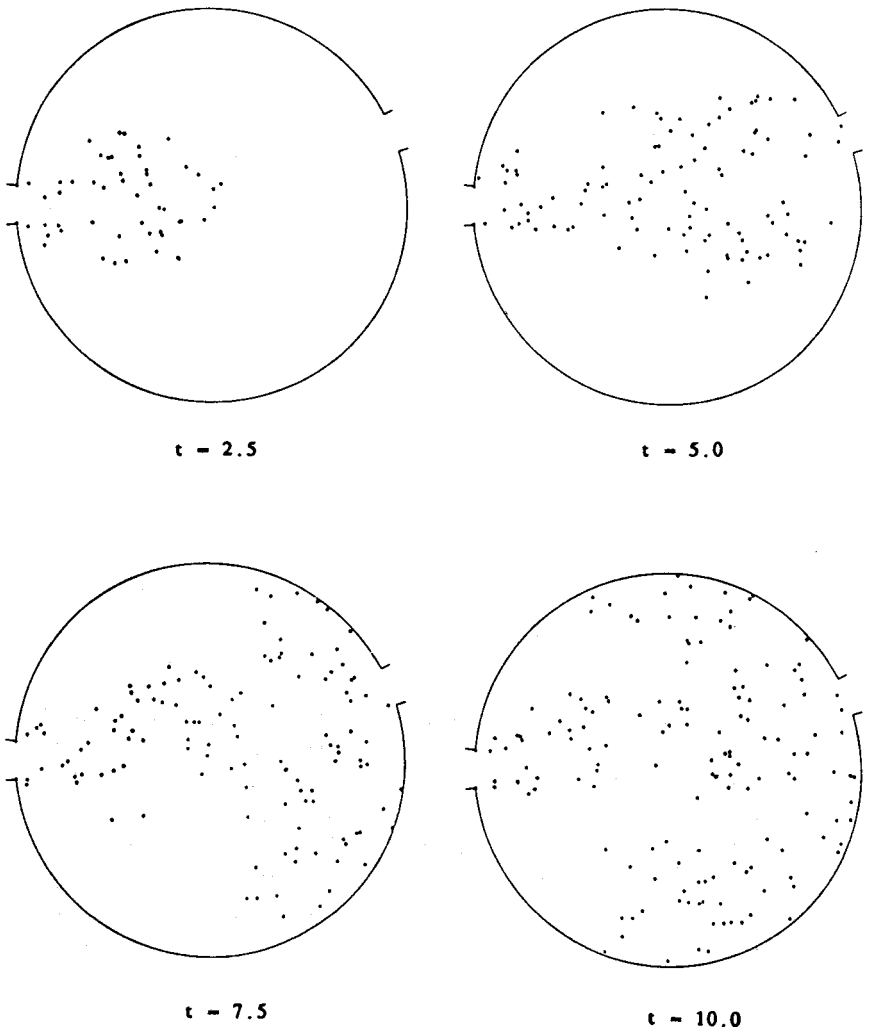

Figure 11. Vortex positions: Rankine vortex simulation with random walk ($r_0 = 0{\cdot}05$, $Re_1 = 100{\cdot}0$)

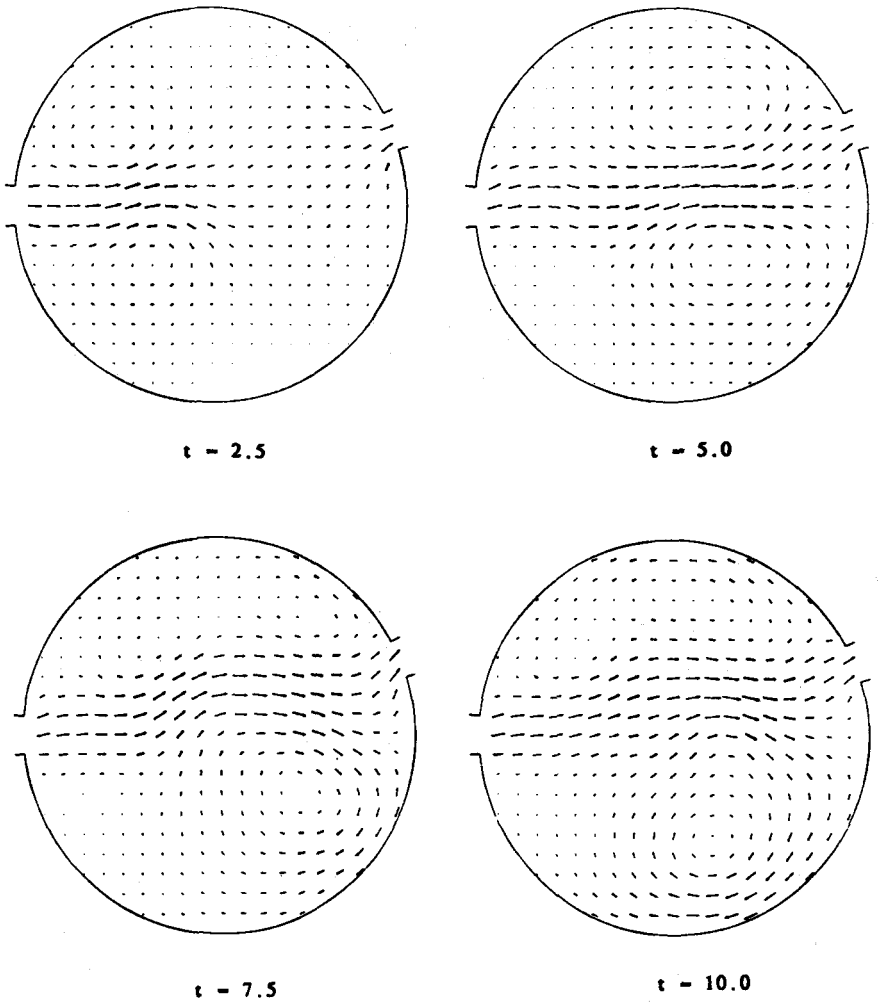

Figure 12. Velocity distributions: Rankine vortex simulation with random walk ($r_0 = 0{\cdot}05$, $Re_i = 100{\cdot}0$)

behave chaotically, the velocity vector plots (Figure 12) are notable for their smooth variation in time. In fact, the random walk mechanism improves the simulation by reducing the circulation of the lower gyre whilst increasing the strength of the upper recirculation zone. Apart from the wavering motion of the main throughflow, the velocity vectors at $t = 10{\cdot}0$ are judged to be in qualitative agreement with the experimental flow visualization illustrated in Figure 13. Beyond $t = 10{\cdot}0$ the inflow jet in the numerical scheme becomes increasingly distorted by the growth of the lower gyre. This leads to a totally unrealistic reservoir circulation pattern as the throughflow is forced towards the upper boundary of the reservoir.

CONCLUSIONS

This paper has described a discrete vortex model for qualitatively assessing jet-forced circulation patterns in circular tanks and reservoirs. First a two-stage conformal mapping is employed to

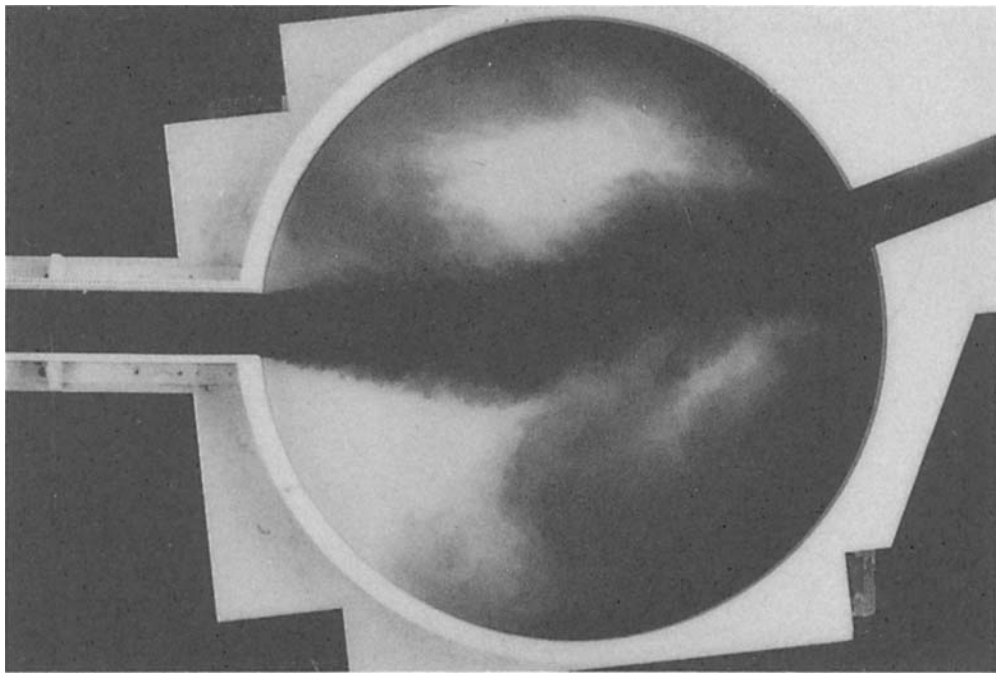

Figure 13. Flow visualization of recirculating eddies in a circular reservoir using potassium permanganate solution (reservoir diameter 1·5 m, flow depth 120 mm, inflow velocity 0·1 m s^{-1})

transform the circular flow domain onto a rectangle; this enables the irrotational flow within the circular reservoir to be determined via an exact analytical technique. In the second stage of the model discrete vortices are superimposed on the irrotational flow solution in order to model the shear layers which are formed either side of the inflow jet. The velocities of the individual vortices are calculated using the 'direct summation' (Biot–Savart) method and consequently the computer time required to update the vorticity field increases rapidly as new vortices are added at the inlet. By restricting the maximum number of vortices to approximately 200, it was found that just under 4 h of CPU time were required on a PR1ME 9955 computer to run the flow simulation to the non-dimensionalized time $t = 10{\cdot}0$. The use of only 200 vortices meant that the discretization of the vorticity field was rather coarse. Nevertheless, the results demonstrate that the model is capable of qualitatively predicting the recirculatory features of momentum-driven reservoir flow.

The most satisfactory flow predictions are obtained when the Lagrangian vortex-tracking algorithm implements a stochastic diffusion model; the random walk mechanism effectively calms the velocity field and reduces the distortions of the throughflow jet. However, in a similar manner to other discrete vortex simulations[4] the present numerical scheme fails to reach steady state or limit cycle conditions, but instead produces an increasingly chaotic flow solution. For this particular model the onset of the chaotic motion is characterized by unrealistically high velocities in the lower recirculation zone. The growth in circulation of the lower eddy may be partially attributed to the fact that the numerical scheme does not account for the generation of vorticity within the boundary layers of the circular perimeter walls. Consequently, it is recommended that future investigations should study the possibilities of adding nascent vortices along the circular

walls of the flow domain as well as at the inlet separation points. This should be implemented as part of a vortex-in-cell model in order to cope with the increased number of elemental vortices. Moreover, the use of transformation techniques, such as proposed by Barfield[34] or Thompson *et al.*,[35–37] is recommended to enable discrete vortex simulations of flow patterns in irregularly shaped reservoirs.

ACKNOWLEDGEMENT

R. W. B. would like to acknowledge support from the U.K. Science and Engineering Research Council.

REFERENCES

1. H. Helmholtz, 'Uber integrale der hydrodynamischen gleichungen weiche den wirbelbewegungen entsprechen', *Crelle-Borchardt, J. Reine angew. Math., Berlin*, **LV**, 25–55 (1858).
2. L. Rosenhead, 'The formation of vortices from a surface discontinuity', *Proc. R. Soc. A*, **134**, 170–192 (1931).
3. R. R. Clements and D. J. Maull, 'The representation of sheets of vorticity by discrete vortices', *Prog. Aerospace Sci.*, **16**, 129–146 (1975).
4. T. Sarpkaya, 'Computational methods with vortices—The 1988 Freeman Scholar Lecture', *J. Fluids Eng.* **111**, 5–52 (1989).
5. G. D. Birkhoff and J. Fisher, 'Do vortex sheets roll up?' *Rc. Circ. Math. Palermo. Ser. 2*, **8**, 77–90 (1959).
6. F. L. Westwater, 'The rolling up of a surface of discontinuity behind an airfoil of infinite span', *ARC R&M 1692*, 1935.
7. H. Takami, 'Numerical experiment with discrete vortex approximation, with reference to the rolling up of a vortex sheet', *Department of Aeronautics and Astronautics, Stanford University Rep. SUDAER 202*, 1964.
8. D. W. Moore, 'The discrete vortex approximation of a finite vortex sheet', *California Institute of Technology Rep. AFOSR-1804-69*, 1971.
9. K. Kuwahara and H. Takami, 'Numerical studies of two-dimensional vortex motion by a system of point vortices', *J. Phys. Soc. Jpn.*, **34**, 247–253 (1973).
10. R. R. Clements and D. J. Maull, 'The rolling up of a trailing vortex sheet', *J. R. Aeronaut Soc.*, **77**, 46–51 (1973).
11. D. W. Moore, 'A numerical study of the roll-up of a finite vortex sheet', *J. Fluid Mech.*, **63**, 225–235 (1974).
12. F. H. Abernathy and R. E. Kronauer, 'The formation of vortex streets', *J. Fluid Mech.*, **13**, 1–20 (1962).
13. J. H. Gerrard, 'Numerical computation of the magnitude and frequency of the lift on a circular cylinder', *Phil. Trans. R. Soc. A*, **261**, 137–162 (1967).
14. T. Sarpkaya, 'An analytical study of separated flow about circular cylinders', *Trans. ASME, J. Basic Eng.*, **90**, 511–520 (1968).
15. A. D. K. Laird, 'Eddy formation behind circular cylinders', *J. Hydraul. Div., Proc. ASCE*, **97**, 763–775 (1971).
16. J. R. Chaplin, 'Computer model of vortex shedding from a cylinder', *J. Hydraul. Div., Proc. ASCE*, **99**, 155–165 (1973).
17. P. K. Stansby, 'An inviscid model of vortex shedding from a circular cylinder in steady and oscillatory far flows', *Proc. Inst. Civil Eng., Pt. 2*, **63**, 865–880 (1977).
18. T. Sarpkaya and R. L. Schoaff, 'Inviscid model of two-dimensional vortex shedding by a circular cylinder', *AIAA J.*, **17**, 1193–1200 (1979).
19. R. R. Clements, 'An inviscid model of two-dimensional vortex shedding', *J. Fluid Mech.*, **57**, 321–336 (1973).
20. A. J. Chorin and P. S. Bernard, 'Discretisation of a vortex sheet, with an example of roll-up', *J. Comput. Phys.*, **13**, 423–429 (1973).
21. G. R. Baker, 'The 'Cloud in.Cell' technique applied to the roll up of vortex sheets', *J. Comput. Phys.*, **31**, 76–95 (1979).
22. P. K. Stansby and A. G. Dixon, 'Simulation of flows around cylinders by a Lagrangian vortex scheme', *Appl. Ocean Res.*, **5**, 167–178 (1983).
23. P. A. Smith and P. K. Stansby, 'Generalized discrete vortex method for cylinders without sharp edges', *AIAA J.*, **25**, 199–200 (1987).
24. A. G. L. Borthwick, J. R. Chaplin and K. H. M. Ali, 'Discrete vortex model of jet-forced flow in a circular reservoir', *J. Hydraul. Eng. (ASCE)*, **114**, 283–298 (1988).
25. S. C. R. Dennis, 'Application of the series truncation method to two-dimensional internal flows', *Proc. 4th Int. Conf. on Numerical Methods in Fluid Dynamics*, Springer, New York, 1974, pp. 146–151.
26. R. D. Mills, 'Computing internal viscous flow problems for the circle by integral methods', *J. Fluid Mech.*, **79**, 609–624 (1977).
27. R. A. Falconer, 'Mathematical modelling of jet-forced circulation in reservoirs and harbours', *Ph.D. Thesis*, Imperial College, London, 1976.
28. R. A. Falconer, 'Numerical modelling of tidal circulation in harbours', *J. Waterway, Port, Coastal Ocean Div., Proc. ASCE*, **106**, 31–48 (1980).

29. A. G. L. Borthwick and R. W. Barber, 'Prediction of low Reynolds number jet-forced flow inside a circle using the Navier–Stokes equations', *Int. J. Eng. Fluid Mech.*, **3**, 323–343 (1990).
30. P. F. Byrd and M. D. Friedman, *Handbook of Elliptic Integrals for Engineers and Physicists*, Springer, New York, 1954.
31. L. M. Milne-Thomson, *Theoretical Hydrodynamics*, 5th edn, Macmillan, New York, 1968.
32. A. J. Raudkivi and R. A. Callander, *Advanced Fluid Mechanics*, Edward Arnold, London, 1975.
33. A. J. Chorin, 'Numerical study of slightly viscous flow', *J. Fluid Mech.*, **57**, 785–796 (1973).
34. W. D. Barfield, 'Numerical method for generating orthogonal curvilinear meshes', *J. Comput. Phys.*, **5**, 23–33 (1970).
35. J. F. Thompson, F. C. Thames and C. W. Mastin, 'Automatic numerical generation of body-fitted curvilinear coordinate system for field containing any number of arbitrary two-dimensional bodies', *J. Comput. Phys.*, **15**, 299–319 (1974).
36. J. F. Thompson, F. C. Thames and C. W. Mastin, 'TOMCAT—a code for numerical generation of boundary-fitted curvilinear coordinate systems on fields containing any number of arbitrary two-dimensional bodies', *J. Comput. Phys.*, **24**, 274–302 (1977).
37. J. F. Thompson, F. C. Thames and C. W. Mastin, 'Boundary-fitted curvilinear coordinate systems for solution of partial differential equations on fields containing any number of arbitrary two-dimensional bodies', *NASA Rep. CR-2729*, National Aeronautics and Space Administration, Washington, DC, 1977.